



Cite this: *Nanoscale*, 2017, **9**, 4707

## Spatially composition-modulated two-dimensional $WS_{2x}Se_{2(1-x)}$ nanosheets†

Xueping Wu,<sup>‡a</sup> Honglai Li,<sup>‡a</sup> Hongjun Liu,<sup>‡a</sup> Xiujuan Zhuang,<sup>a</sup> Xiao Wang,<sup>a,b</sup> Xiaopeng Fan,<sup>a</sup> Xidong Duan,<sup>a</sup> Xiaoli Zhu,<sup>a</sup> Qinglin Zhang,<sup>a</sup> Alfred J. Meixner,<sup>b</sup> Xiangfeng Duan<sup>c</sup> and Anlian Pan<sup>id</sup>\*<sup>a</sup>

Controllable synthesis of two-dimensional (2D) transition-metal dichalcogenides (TMDs) with tunable bandgaps is vital for their applications in nanophotonics, due to its efficient modulation of the physical and chemical properties of these atomic layered nanostructures. Here we report for the first time, the controllable synthesis of spatially composition-modulated  $WS_{2x}Se_{2(1-x)}$  nanosheets and  $WS_2-WS_{2x}Se_{2(1-x)}$  lateral heterostructures by a developed one-step chemical vapor deposition (CVD) approach, as well as the understanding of their growth mechanism. During the growth, the composition was optically tuned along the plane of the atomic layered nanosheets through the precise control of evaporation sources. Microstructure characterization confirms the chemical identity of the composition modulated nanosheets, with S and Se contents gradually converting from the center to the edge. Local photoluminescence (PL) and Raman studies further demonstrate the position-dependent optical properties of the as-grown nanosheets, with the PL peak and Raman modes shifting in a wide range along the whole plane of the nanostructures, which are consistent with their tunable compositions and bandgaps. This demonstration of composition-modulated nanostructures provides a beneficial approach for the preparation of 2D semiconductor heterostructures and may open up a wide range of applications in nanoelectronics and optoelectronics.

Received 12th January 2017,  
Accepted 5th March 2017

DOI: 10.1039/c7nr00272f

rsc.li/nanoscale

## Introduction

Since the first successful realization of graphene by mechanical exfoliation in 2004,<sup>1</sup> two-dimensional (2D) materials, especially transition metal dichalcogenide (TMD) semiconductors, have attracted considerable attention due to their unique optical and electrical properties and tremendous application values in the past few years.<sup>2–25</sup> As is known, the application of semiconductor materials is closely related to their bandgaps/compositions,<sup>26–30</sup> an important task in the research of TMDs is to precisely control the bandgaps/compositions of the resulting materials to realize the desired function for

potential applications in electronic/optoelectronic devices. Alloy structures and heterostructures are two effective ways to realize precise modulation of the electronic structures of TMDs.<sup>31–34</sup> To date, lots of TMD alloys with homogeneous compositions have been synthesized, and the preparation of TMD heterostructures has also achieved great progress during the past few years, both of which already brought big innovations in the field of nanoelectronics, optoelectronics, and photonics.<sup>35–42</sup> Thus, realization of heterostructures and the bandgap-modulated alloys within a single TMD nanostructure is of great significance in preparing 2D high-performance or new multifunctional 2D nanodevices, which would be a great benefit for the future development of integrated devices and systems.

As important TMD semiconductors with better optical performance, atomic layered  $WS_2$  and  $WSe_2$  have strong photoluminescence at room temperature with the spectral peak positions at  $\sim 640$  and  $\sim 760$  nm, respectively. Meanwhile, the similarity of the atomic structure between  $WS_2$  and  $WSe_2$  makes them very easy to form alloyed structures, and the composition of the alloys can be optically modulated as theoretically predicted,<sup>43</sup> which provides a vital basis for the preparation of composition-modulated alloy nanosheets and heterostructures. Here, we report the controllable synthesis of spatially composition-modulated  $WS_{2x}Se_{2(1-x)}$  nanosheets and

<sup>a</sup>Key Laboratory for Micro-Nano Physics and Technology of Hunan Province, School of Physics and Electronic Science, and State Key Laboratory of Chemo/Biosensing and Chemometrics, Hunan University, Changsha, Hunan 410082, P. R. China.

E-mail: anlian.pan@hnu.edu.cn

<sup>b</sup>Institute of Physical and Theoretical Chemistry and LISA+, University of Tübingen, Auf der Morgenstelle 18, 72076 Tübingen, Germany

<sup>c</sup>Department of Chemistry and Biochemistry, University of California, Los Angeles, CA 90095, USA

†Electronic supplementary information (ESI) available: CVD setup and AFM and Raman mode shift of single-way  $WS_{2x}Se_{2(1-x)}$ , and Raman spectra of  $WS_{2x}Se_{2(1-x)}$ . See DOI: 10.1039/c7nr00272f

‡These authors contributed equally to this work.

$WS_2$ - $WS_{2x}Se_{2(1-x)}$  lateral heterostructures through a developed source-moving chemical vapor deposition (CVD) method, with the composition optically tuned along the plane of the achieved nanosheets. From the center to the edge of a single nanosheet, the chemical composition can not only be gradually tuned single-way or both-way as desired, but can also be sharply tuned to form lateral heterostructures. Structural and optical studies demonstrate the composition modulation of the sheets, which exhibit composition/position-dependent band edge emission and Raman mode shifting. These new 2D semiconductor nanostructures may have potential applications in integrated nanoelectronics and nanophotonics.

## Experimental

### Synthesis

A home-built optimized CVD system was used.<sup>44–48</sup> A quartz boat loaded with  $WS_2$  powder was loaded at the center of the furnace, and another boat loaded with Se powder was placed in the upstream areas, which is far enough to the heating area and can be shifted by a quartz rod driven by a step motor through the magnetic force during the growth [Fig. S1(a)†]. A long piece of  $SiO_2/Si$  wafer (oxide thickness of  $\sim 300$  nm) was placed in the downstream of the furnace to collect the deposited samples. Before heating, an Ar gas flow was introduced into the system for 10 min in order to exhaust the air and maintain the flow at 70 standard-state cubic centimeter per minute (scm). The furnace was then rapidly heated to 1100 °C in 35 min, and slowly heated to 1150 °C in 5 min. After keeping the growth at this temperature for several minutes, the furnace was then cooled down to room temperature naturally.

### Characterization

Structures, morphologies and compositions of the samples were characterized with optical microscopy, Raman spectroscopy (WITec, alpha-300, 532 nm excitation), atomic force microscopy (AFM) (Bruker Multimode 8) and transmission electron microscopy (TEM) (FEI F20, voltage: 300 kV).

## Results and discussion

Fig. 1 shows schematic diagrams. The  $WS_2$  triangular nanosheets are firstly synthesized to act as the seed for the followed lateral growth of the 2D TMD nanostructures. During the lateral growth, the heating temperature of the Se source can be precisely controlled through the source-moving of the Se source according to different fashions to obtain different structures, including single-way composition graded structure (I), both-way composition graded structure (II) and composition graded heterostructure (III). For structure I, the heating temperature of the Se source is continually increased, covering the whole lateral growth process. For structure II, the heating temperature of the Se source is first increased and then decreased during the growth, while for structure III, the Se source only

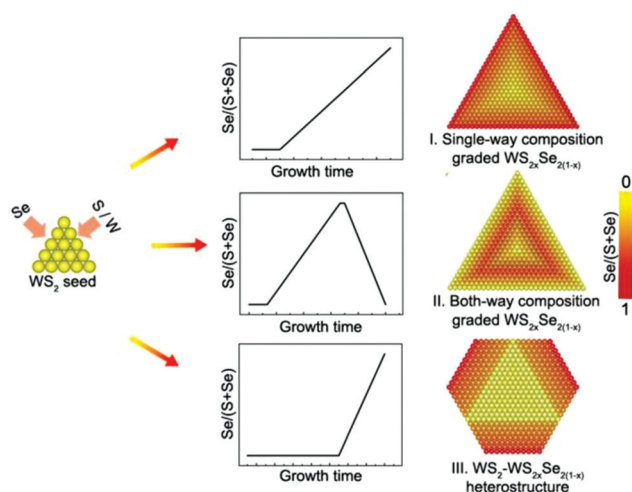


Fig. 1 Schematic diagrams for the growth of single-way composition graded  $WS_{2x}Se_{2(1-x)}$  (I), both-way composition graded  $WS_{2x}Se_{2(1-x)}$  (II) and composition graded  $WS_2$ - $WS_{2x}Se_{2(1-x)}$  heterostructured (III) nanosheets, respectively.

begins to evaporate after the  $WS_2$  has grown big enough at the late stage of the growth. More experimental details of the growth are presented in the ESI.† Photoluminescence (PL) and Raman spectra were used to characterize the position-dependent optical and structural modulations of these nanosheets, which were conducted using a confocal Raman system (WITec, alpha-300) with Ar ion laser (532 nm) excitation.

Fig. 2a shows an optical image of a representative sample of structure I, which exhibits a typical triangular like morphology. Fig. 2b shows the position-dependent PL spectra collected at five different positions from the center to the edge of a typical nanosheet (see the markers in Fig. 2a) with a

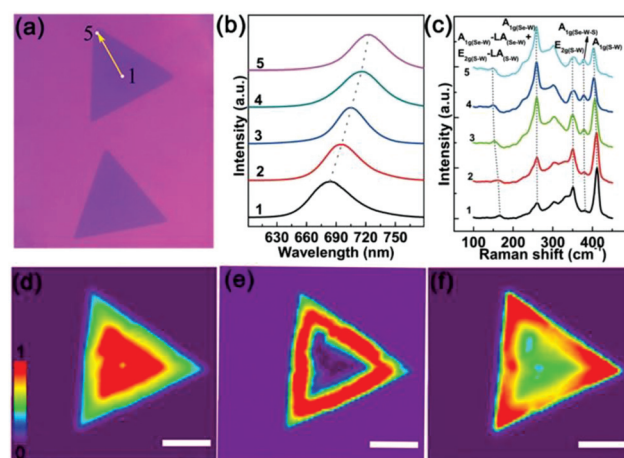
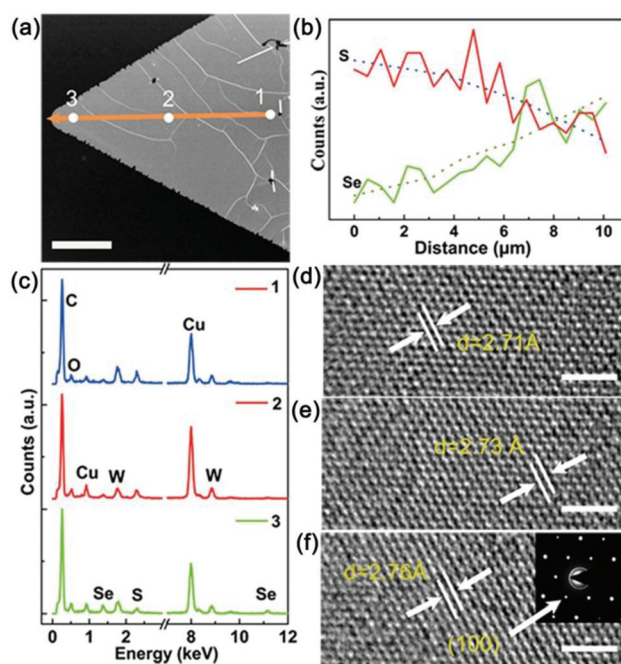


Fig. 2 (a) Microscopic optical image of two as-grown single-way composition graded  $WS_{2x}Se_{2(1-x)}$  nanosheets (scale bar, 2  $\mu m$ ), (b, c) position-dependent PL and micro-Raman spectra of the nanosheet (see the markers in (a)), respectively, and (d–f) the corresponding wavelength-dependent PL mappings in the spectral regions of 685–695 nm, 700–710 nm, 715–725 nm, respectively (scale bar, 3  $\mu m$ ).

uniform thickness of 2.15 nm, which indicates the trilayer character of the sheet (Fig. S2†). All the spectra reveal single emission bands, with the peak wavelength gradually shifted from 685 nm at the center to 725 nm at the edge, which is well consistent with the observed composition-dependent band edge emission of TMD alloys.<sup>20</sup> The gradual shift of PL peak positions indicates that the as-grown nanostructures are composition modulated in the lateral direction. In addition to the PL spectra, Raman spectra from the same nanosheet were also collected. Fig. 2c shows the normalized position-dependent Raman spectra of the sheet, scanning from the center (curve 1) to the edge (curve 5), which display five main modes for most  $WS_{2x}Se_{2(1-x)}$  nanosheets, which can be assigned to  $A_{1g(S-W)}$  mode (402–413  $cm^{-1}$ ),  $A_{1g(Se-W)}$  mode (258–261  $cm^{-1}$ ),  $E_{2g(S-W)}$  mode (349–351  $cm^{-1}$ ),  $A_{1g(S-W-Se)}$  mode (377–382  $cm^{-1}$ ), and  $E_{2g(S-W)} - LA_{(S-W)} + A_{1g(Se-W)} - LA_{(Se-W)}$  mode, respectively. All the vibration modes shift to low frequency with relative intensity evolution from positions 1 to 5 (see ESI Fig. S3†). For example, with the detection moving from the center to the edge, the  $A_{1g(S-W)}$  mode shows a clear shift from 411.8  $cm^{-1}$  to 402.8  $cm^{-1}$ , with the intensity gradually decreased from the center toward the edge, and the  $E_{2g(S-W)} - LA_{(S-W)} + A_{1g(Se-W)} - LA_{(Se-W)}$  mode, the superposition of  $A_{1g(Se-W)} - LA_{(Se-W)}$  and  $E_{2g(S-W)} - LA_{(S-W)}$  also shows a systematic shift from 165.7  $cm^{-1}$  to 148.0  $cm^{-1}$ , which is unique for  $WS_{2x}Se_{2(1-x)}$  alloy nanosheets,<sup>32</sup> well confirming that the nanosheet is the single-way graded  $WS_{2x}Se_{2(1-x)}$ . This transition of the molecular vibration modes shows good agreement with the continuously modulated composition of the nanosheet. Fig. 2d–f show the wavelength-selected PL mapping of the examined nanosheet in the spectral regions of 685–695 nm, 700–710 nm and 715–725 nm, respectively. Obviously, the short wavelength area (685–695 nm) is mainly located at the center of the sheet, while the long wavelength area (715–725 nm) is mostly located around the edge of the structure. This observation agrees well with the above results from position-dependent PL measurements, and further demonstrates that the alloy nanostructures are composition graded along the whole plane of the sheet from the center to the edge.

Transmission electron microscopy (TEM) were used to further study the structure and composition characteristics of the achieved nanosheets. Fig. 3a shows a typically rough TEM image of a single-way composition graded  $WS_{2x}Se_{2(1-x)}$  nanosheet. Fig. 3b shows the energy dispersive X-ray (EDX) spectroscopy spectra collected from three selected positions along the arrow (points 1–3 in Fig. 3a), indicating that the nanosheet is composed of the elements S, Se, and W, and the ratio of S/Se decreases gradually from positions 1 to 3, confirming the existence of a laterally graded composition within the as-grown nanosheets. Fig. 3c shows the energy dispersive X-ray spectroscopy (EDS) line scan profiles of the elemental distribution along the indicated arrow from the center to the edge of the triangle area, as shown in Fig. 3a, which shows that S is located more at the center region and is gradually reduced from the center to the edge of the nanosheet, while Se shows the opposite trend with a gradually increased content.



**Fig. 3** (a) Typical TEM image of a single-way composition graded  $WS_{2x}Se_{2(1-x)}$  nanosheet (scale bar, 1.5  $\mu m$ ) and (b) the corresponding TEM-EDX profiles recorded at three selected positions (1–3) in the sheet. (c) EDS line scan profiles of S and Se distributions, showing the opposite variation trend from the center to the edge of the sample. (d–f) The HRTEM images taken from the three different positions (scale bars, 2 nm). Inset of (f) the SAED pattern of the nanosheets.

Fig. 3d–f show the high-resolution transmission electron microscopy (HRTEM) images taken from the three different positions along the nanosheet, corresponding to the positions for the EDS analysis (see Fig. 3b), which shows that all the examined positions are highly crystallized, with the measured lattice plane spacing of 2.71, 2.73, and 2.76  $\text{\AA}$ , respectively, in agreement with the spacing between two neighboring (100) planes of the composition modulated atomic layered  $WS_{2x}Se_{2(1-x)}$  alloys.<sup>26</sup> The inset of Fig. 3f is the selected area electron diffraction (SAED) pattern of the sheet, which shows a clearly defined single set of diffraction spots, further demonstrating the single-crystalline nature of the achieved 2D structures without significant defects.

Based on the above achievement of single-way composition modulation from the center to the edge of the  $WS_{2x}Se_{2(1-x)}$  nanosheets (structure I), both-way composition graded  $WS_{2x}Se_{2(1-x)}$  alloys (structure II) can also be achieved by controlling the heating temperature of the Se source in a different fashion, *i.e.* it is first increased and then decreased during the growth (see the experimental details in the ESI†). Fig. 4a shows a typical optical image of the as-grown both-way composition graded  $WS_{2x}Se_{2(1-x)}$  nanosheets, with a uniform thickness of 1.75 nm, which indicates the bilayer character of the sheet (Fig. S4†). Fig. 4b shows the position-dependent PL spectra of the sample, collected locally from five positions from the center (point 1) to the edge (point 5) marked in

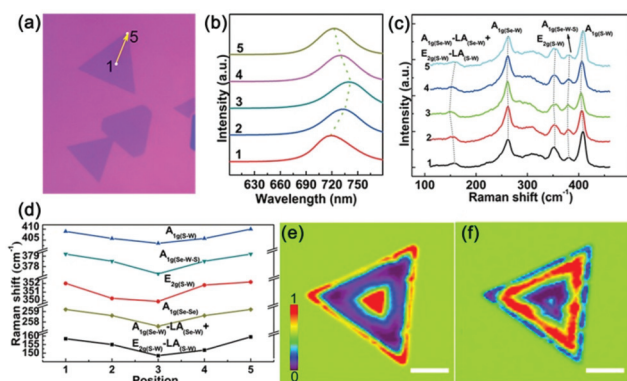


**Fig. 4** (a) Microscopic optical image of both-way composition graded  $WS_{2x}Se_{2(1-x)}$  nanosheets (scale bar, 3  $\mu\text{m}$ ). (b, c) Position-dependent PL and micro-Raman spectra of the nanosheet indicated by the arrow in (a), respectively, and (d) their corresponding Raman mode shift with the positions. (e, f) The wavelength-selected PL mapping in the spectral regions of 715–725 nm, 735–745 nm, respectively (scale bar, 2  $\mu\text{m}$ ).

Fig. 4a. The results show that the PL peak wavelength is first gradually red-shifted from 718 nm (curve 1) to 742 nm (curve 3), and then blue-shifted back to 722 nm (curve 5), which indicates that the composition of the nanosheets is both-way modulated, with the Se/S ratio first increased and then decreased from the center to the edge of the nanostructure. The formation of both-way composition graded  $WS_{2x}Se_{2(1-x)}$  nanosheets was further confirmed by the composition-dependent vibration modes observed from the micro-Raman measurements, as shown in Fig. 4c and d. The results show that the intensities of Se–W related modes are gradually increased and then decreased from the center to the edge of the sheet, while the intensities of S–W related modes are first decreased and then increased (Fig. 4d), and all the observed vibration modes shift towards low frequency and then move back to high frequency from the center to the edge (Fig. 4c). The intensity and frequency shifting of the vibration modes demonstrate that the both-way structural evolution is attributed to the composition graded modulation in the sheet. Fig. 4e and f show the wavelength-selected PL emission mappings of the examined nanosheet in the spectral regions of 715–725 nm and 735–745 nm, respectively, showing that the short wavelength region is located at both the center and the edge of the nanosheet, while the long wavelength region is mostly located between the center and the edge. This observation further demonstrates that the  $WS_{2x}Se_{2(1-x)}$  alloy sample is both-way composition graded along the whole plane of the sheet from the center to the edge.

More importantly, the composition modulated growth can be further extended to realize composition graded  $WS_2$ – $WS_{2x}Se_{2(1-x)}$  heterostructures (structure III) by forming a  $WS_2$  triangle before the evaporation of the Se source (see the experimental details in the ESI<sup>†</sup>), and the optical image of the achieved structures is shown in Fig. 5a, with the thicknesses of 1.75 nm (edge) and 2.4 nm (center) as shown in Fig. S5.† Fig. 5b and c show the wavelength-selected PL mapping of the

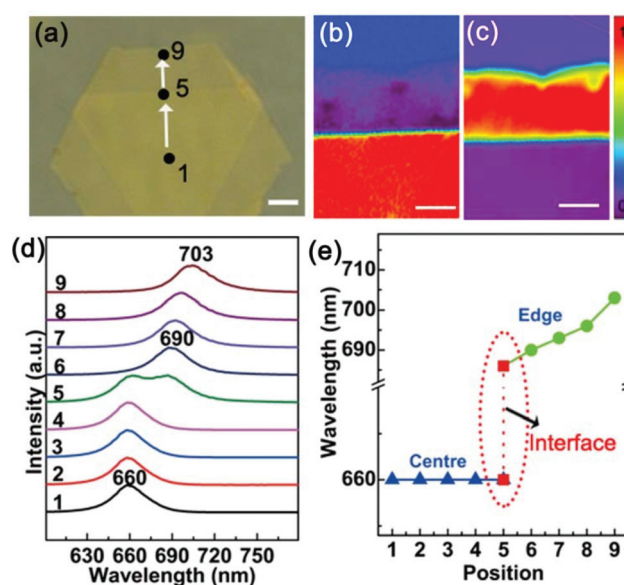


**Fig. 5** (a) Microscopic optical image of the  $WS_2$ – $WS_{2x}Se_{2(1-x)}$  heterostructure (scale bar, 5  $\mu\text{m}$ ). (b, c) Wavelength-dependent PL mapping of the selected area in (a) in the spectral regions of 660 nm, 690–703 nm, respectively (scale bar, 2  $\mu\text{m}$ ). (d) Position-dependent PL spectrum of a  $WS_2$ – $WS_{2x}Se_{2(1-x)}$  lateral heterostructure. (e) The PL peak change trend along the arrow in (a).

selected area in the examined nanosheet (see the indicated selected region in Fig. 5a) in the spectral regions of 660 nm, and 690–703 nm, respectively, with the bottom part consisting of a small part of  $WS_2$  (Fig. 5b) and the middle part consisting of the  $WS_{2x}Se_{2(1-x)}$  alloy (Fig. 5c). Fig. 5d shows the PL spectra of the  $WS_2$ – $WS_{2x}Se_{2(1-x)}$  heterostructured nanosheet, with nine curves collected from positions 1 to 9 in a single sheet (see the arrow in Fig. 5a). The peak wavelength of the emission band at the central region (positions 1–4) is always consistent with the near-band-edge energy of  $WS_2$  (660 nm), while the peak wavelength at the peripheral region (positions 6–9) is gradually red-shifted from 686 nm to 703 nm. The spectra collected at the interface region (position 5) exhibit two peaks, which come from the emission of both the central and peripheral regions simultaneously, indicating the heterostructure nature of the nanosheet. The modulation of the PL peak position can be more clearly seen in Fig. 5e, which reveals a sharp interface at position 5, further demonstrating that the achieved nanosheet is the  $WS_2$ – $WS_{2x}Se_{2(1-x)}$  heterostructure. The changelessness of Raman spectra from positions 1 to 4 and the gradient change from positions 5 to 9 agree well with the above conclusion from PL measurements (ESI Fig. S6<sup>†</sup>).

From the above reported growth and characterization, it can be noted that 2D composition graded  $WS_{2x}Se_{2(1-x)}$  alloy structures and  $WS_2$ – $WS_{2x}Se_{2(1-x)}$  heterostructures can be achieved by selectively controlling the evaporation of Se sources. At the beginning of the growth for the structures I and II,  $WS_2$  nucleates on the  $SiO_2$  substrate, forming the seed for the followed lateral growth of the composition graded 2D alloy nanostructures. Then, the edges of the pre-grown  $WS_2$

seeds act as the active nucleation sites due to the existence of dangling bonds, leading to the lateral extension growth of the nanosheets. After the Se powder starts to evaporate, the evaporated Se vapour will be brought by the carrier gas to the heating center. Then, the Se atoms react with the WS<sub>2</sub> flux at the center of the furnace and partially substitute the S atoms in the WS<sub>2</sub> molecules before nucleating at the edge sites of the growing seeds, resulting in the growth of the composition graded WS<sub>2</sub>xSe<sub>2(1-x)</sub> alloy in the lateral direction of the nanosheets (structure I). As the concentration of Se increases with the time, more and more S atoms in WS<sub>2</sub> molecules in the vapor will be substituted by Se atoms, leading to the increasing ratio of Se in the alloy structures. If the Se precursor atoms first increase and then decrease (*via* the control of the heating temperature of Se powder) in the process of the growth for the nanostructures, it would lead to the composition modulating forth and back in the lateral direction of the sheet (structure II). In the above two growth cases, as the WS<sub>2</sub> clusters have high chemical activity and easy to react with the Se vapor to form alloy seeds, the composition for the as-grown seeds can be tuned by conducting the Se vapor at the initial growth process. If the WS<sub>2</sub> nanoclusters have been grown to a relatively large size nanosheet before the Se powder starts to evaporate, the pre-formed WS<sub>2</sub> can work as a stable core (see the central triangular in Fig. 5a) for the followed growth of the high Se composition. Besides, S dimers can easily form in a large size WS<sub>2</sub> nanosheet, which will increase the energy barrier for the substitution of S atoms.<sup>49</sup> Therefore, it is easy to form the interface in the growth process III (see Fig. 1), and achieve the composition graded heterostructure (structure III). Meanwhile, the existence of S dimers will help to form the inversion domain boundaries as reported.<sup>50,51</sup> Because of the lattice difference between WS<sub>2</sub> and WSe<sub>2</sub>, the formation of the domain boundaries at the interface can stabilize the nanosheet. The formation of such kinds of domain boundaries will change the atomic structure of the growing edges, for example, from the zig-zag structure to the armchair structure, which will lead to the change of the direction of the growth, as shown in Fig. 5a. The continuous growth of the lateral WS<sub>2</sub>-WS<sub>2</sub>xSe<sub>2(1-x)</sub> heterostructures would realize the growth of alloy structures and heterostructures in a single sample. If we precisely control the evaporation of the Se source, we can grow periodic structures of modulated alloy structures and heterostructures in the same chip. Such a simple control will bring great benefit to the development of the integrated nanoelectronic devices.

## Conclusions

In conclusion, spatially composition-modulated WS<sub>2</sub>xSe<sub>2(1-x)</sub> nanosheets have been successfully grown using a developed moving-source chemical vapor deposition method. Through the *in situ* controlling of the evaporation rate of the Se source during the lateral epitaxial process, the composition along the lateral direction of the nanosheets can be continuously tuned

from WS<sub>2</sub> towards WSe<sub>2</sub> and even tuned back, or sharply tuned from WS<sub>2</sub> to WS<sub>2</sub>xSe<sub>2(1-x)</sub> alloy, forming single-way composition graded structure (I), both-way composition graded structure (II) and composition graded heterostructure (III). Optical measurements demonstrate that these composition-modulated nanosheets can give position-related PL emission, with the peak wavelength optically tuned between 660 nm and 745 nm. The simple and precise preparation of such composition modulated 2D alloy nanostructures could find significant applications in fundamental physical research and the construction of functional electronic and photovoltaic devices.

## Author contributions

X. P. W., H. L. L. and H. J. L. designed and performed experiments, and wrote the manuscript. X. J. Z., X. P. F. and Q. L. Z. advised on optical measurements, X. D. D. and X. L. Z. advised on materials preparation. X. W., A. J. M. and X. F. D. advised on data analysis. A. L. P. advised on designing the experiments and analyzing the results, and provided theoretical guidance. All authors discussed results, commented on them, and edited.

## Acknowledgements

The authors are grateful to the National Natural Science Foundation of China (no. 11374092, 61474040, 61574054, and 61505051), the Aid Program for Science and Technology Innovative Research Team in Higher Educational Institutions of Hunan Province, the Hunan Provincial Science and Technology Department (no. 2014FJ2001, 2014GK3015, and 2014TT1004), the Joint Research Fund for Overseas Chinese, Hong Kong and Macau Scholars of the National Natural Science Foundation of China (no. 61528403), Overseas and Hong Kong and Macao Scholars Cooperative Research Fund (no. 61528403) and the doctoral student research innovation project of Hunan province (no. CX2015B071).

## Notes and references

- 1 K. S. Novoselov, A. K. Geim, S. V. Morozov, D. Jiang, Y. Zhang, S. V. Dubonos, I. V. Grigorieva and A. A. Firsov, *Science*, 2004, **306**, 666–669.
- 2 Q. H. Wang, K. Kalantar-Zadeh, A. Kis, J. N. Coleman and M. S. Strano, *Nat. Nanotechnol.*, 2012, **7**, 699–712.
- 3 X. Duan, C. Wang, A. Pan, R. Yu and X. Duan, *Chem. Soc. Rev.*, 2015, **44**, 8859–8876.
- 4 X. Zhang, X. F. Qiao, W. Shi, J. B. Wu, D. S. Jiang and P. H. Tan, *Chem. Soc. Rev.*, 2015, **44**, 2757–2785.
- 5 Y. Chen, C. Tan, H. Zhang and L. Wang, *Chem. Soc. Rev.*, 2015, **44**, 2681–2701.
- 6 X. Duan, C. Wang, J. C. Shaw, R. Cheng, Y. Chen, H. Li, X. Wu, Y. Tang, Q. Zhang, A. Pan, J. Jiang, R. Yu, Y. Huang and X. Duan, *Nat. Nanotechnol.*, 2014, **9**, 1024–1030.

- 7 O. L. Sanchez, D. Lembke, M. Kayci, A. Radenovic and A. Kis, *Nat. Nanotechnol.*, 2013, **8**, 497–501.
- 8 R. Schmidt, A. Arora, G. Plechinger, P. Nagler, A. G. Aguila, M. V. Ballottin, P. C. M. Christianen, S. M. Vasconcellos, C. Schuller, T. Korn and R. Bratschitsch, *Phys. Rev. Lett.*, 2016, **117**, 077402.
- 9 S. H. Yu, Y. Lee, S. K. Jang, J. Kang, J. Jeon, C. Lee, J. Y. Lee, H. Kim, E. Hwang, S. Lee and J. H. Cho, *ACS Nano*, 2014, **8**, 8285–8291.
- 10 W. J. Yu, Z. Li, H. Zhou, Y. Chen, Y. Wang, Y. Huang and X. Duan, *Nat. Mater.*, 2013, **12**, 246–252.
- 11 C. Huang, S. Wu, A. M. Sanchez, J. J. P. Peters, R. Beanland, J. S. Ross, P. Rivera, W. Yao, D. H. Cobden and X. Xu, *Nat. Mater.*, 2014, **13**, 1096–1101.
- 12 B. W. H. Baugher, H. O. H. Chuechill, Y. Yang and P. Jarillo-Herrero, *Nat. Nanotechnol.*, 2014, **9**, 262–267.
- 13 S. Jo, N. Ubrig, H. Berger, A. B. Kuzmenko and A. F. Morpurgo, *Nano Lett.*, 2014, **14**, 2019–2025.
- 14 D. Sarkar, X. Xie, W. Liu, W. Cao, J. Kang, Y. Gong, S. Kraemer, P. M. Ajayan and K. Banerjee, *Nature*, 2015, **526**, 91–95.
- 15 X. Zhang, Z. Lai, C. Tan and H. Zhang, *Angew. Chem., Int. Ed.*, 2016, **55**, 8816–8838.
- 16 C. Tan, Z. Liu, W. Huang and H. Zhang, *Chem. Soc. Rev.*, 2015, **44**, 2615.
- 17 H. Li, J. Wu, Z. Yin and H. Zhang, *Acc. Chem. Res.*, 2014, **47**, 1067–1075.
- 18 H. Li, X. Wu, H. Liu, B. Zheng, Q. Zhang, X. Zhu, Z. Wei, X. Zhuang, H. Zhou, W. Tang, X. Duan and A. Pan, *ACS Nano*, 2017, **11**, 961–967.
- 19 A. Pant, Z. Mutlu, D. Wickramaratne, H. Cai, R. K. Lake, C. Ozkan and A. Tongay, *Nanoscale*, 2016, **8**, 3870.
- 20 H. Zhang, *ACS Nano*, 2015, **9**, 9451–9469.
- 21 H. Zeng, G. B. Liu, J. Dai, Y. Yan, B. Zhu, R. He, L. Xie, S. Xu, X. Chen, W. Yao and X. Cui, *Sci. Rep.*, 2013, **3**, 1608.
- 22 J. Miao, W. Hu, Y. Jing, W. Luo, L. Liao, A. Pan, S. Wu, J. Cheng, X. Chen and W. Lu, *Small*, 2015, **11**, 2392–2398.
- 23 A. Azizi, X. Zou, P. Ercius, Z. Zhang, A. L. Elias, N. P. Lopez, G. Stone, M. Terrones, B. I. Yakobson and N. Alem, *Nat. Commun.*, 2014, **5**, 4867.
- 24 Y. Zhang, B. Zheng, C. Zhu, X. Zhang, C. Tan, H. Li, B. Chen, J. Yang, J. Chen, Y. Huang, L. Wang and H. Zhang, *Adv. Mater.*, 2014, **26**, 2185–2204.
- 25 T. Shen, A. V. Penumatcha and J. Appenzeller, *ACS Nano*, 2016, **10**, 4712–4718.
- 26 C. Tan and H. Zhang, *Chem. Soc. Rev.*, 2015, **44**, 2713–2731.
- 27 H. P. Komsa and A. V. Krasheninnikov, *J. Phys. Chem. Lett.*, 2012, **3**, 3652–3656.
- 28 H. Li, Q. Zhang, X. Duan, X. Wu, X. Fan, X. Zhu, X. Zhuang, W. Hu, H. Zhou, A. Pan and X. Duan, *J. Am. Chem. Soc.*, 2015, **137**, 5284–5287.
- 29 H. Li, X. Duan, X. Wu, X. Zhuang, H. Zhou, Q. Zhang, X. Zhu, W. Hu, P. Ren, P. Guo, L. Ma, X. Fan, X. Wang, J. Xu, A. Pan and X. Duan, *J. Am. Chem. Soc.*, 2014, **136**, 3756–3759.
- 30 C. Tan and H. Zhang, *J. Am. Chem. Soc.*, 2015, **137**, 12162–12174.
- 31 Q. Zeng, H. Wang, W. Fu, Y. Gong, W. Zhou, P. M. Ajayan, J. Lou and Z. Liu, *Small*, 2015, **11**, 1868–1884.
- 32 X. Li, *Nanoscale*, 2015, **7**, 18392–18401.
- 33 X. Duan, C. Wang, Z. Fan, G. Hao, L. Kou, U. Halim, H. Li, X. Wu, Y. Wang, J. Jiang, A. Pan, Y. Huang, R. Yu and X. Duan, *Nano Lett.*, 2016, **16**, 264–269.
- 34 P. Rivera, J. R. Schaibley, A. M. Jones, J. S. Ross, S. Wu, G. Aivazian, P. Klement, K. Seyler, G. Klark, N. J. Ghimire, J. Yan, D. G. Mandrus, W. Yao and X. Xu, *Nat. Commun.*, 2015, **6**, 6242.
- 35 K. Chen, X. Wan, W. Xie, J. Wen, Z. Kang, X. Zeng, H. Chen and J. Xu, *Adv. Mater.*, 2015, **27**, 6431–6437.
- 36 Y. Gong, J. Lin, X. Wang, G. Shi, S. Lei, Z. Lin, X. Zou, G. Ye, R. Vajtai, B. I. Yakobson, H. Terrones, M. Terrones, B. K. Tay, J. Lou, S. T. Pantelides, Z. Liu, W. Zhou and P. M. Ajayan, *Nat. Mater.*, 2014, **13**, 1135–1142.
- 37 Q. Feng, N. Mao, J. Wu, H. Xu, C. Wang, J. Zhang and L. Xie, *ACS Nano*, 2015, **9**, 7450–7455.
- 38 S. Zheng, L. Sun, T. Yin, A. M. Dubrovkin, F. Liu, Z. Liu, Z. X. Shen and H. J. Fan, *Appl. Phys. Lett.*, 2015, **106**, 063113.
- 39 Y. Gong, Z. Liu, A. R. Lupini, G. Shi, J. Lin, S. Najimaie, Z. Lin, A. L. Elias, A. Berkdemir, G. You, H. Terrones, M. Terrones, R. Vajtai, S. T. Pantelides, S. J. Pennycook, J. Lou, W. Zhou and P. M. Ajayan, *Nano Lett.*, 2014, **14**, 442–449.
- 40 X. Q. Zhang, C. H. Lin, Y. W. Tseng, K. H. Huang and Y. H. Lee, *Nano Lett.*, 2015, **15**, 410–415.
- 41 Q. Feng, Y. Zhu, J. Hong, M. Zhang, W. Duan, N. Mao, J. Wu, H. Xu, F. Dong, F. Lin, C. Jin, C. Wang, J. Zhang and L. Xie, *Adv. Mater.*, 2014, **26**, 2648–2653.
- 42 H. Liu, K. K. A. Ansah, S. Chuaand and D. Chi, *Nanoscale*, 2014, **6**, 624.
- 43 J. Kang, S. Tongay, J. Li and J. Wu, *J. Appl. Phys.*, 2013, **113**, 143703.
- 44 L. Ma, W. Hu, Q. Zhang, P. Ren, X. Zhuang, H. Zhou, J. Xu, H. Li, Z. Shan, X. Wang, L. Liao, H. Q. Xu and A. Pan, *Nano Lett.*, 2014, **14**, 694–698.
- 45 X. Wang, X. Zhuang, F. Wackenhut, Y. Li, A. Pan and A. J. Meixner, *Laser Photonics Rev.*, 2016, **10**, 835–842.
- 46 P. Guo, X. Zhuang, J. Xu, Q. Zhang, W. Hu, X. Zhu, X. Wang, Q. Wan, P. He, H. Zhou and A. Pan, *Nano Lett.*, 2013, **13**, 1251–1256.
- 47 Z. Yang, J. Xu, P. Wang, X. Zhuang, A. Pan and L. Tong, *Nano Lett.*, 2011, **11**, 5085–5089.
- 48 J. Xu, L. Ma, P. Guo, X. Zhuang, X. Zhu, W. Hu, X. Duan and A. Pan, *J. Am. Chem. Soc.*, 2012, **134**, 12394–12397.
- 49 S. Helveg, J. V. Lauritsen, E. Lægsgaard, I. Stensgaard, J. K. Nørskov, B. S. Clausen, H. Topsøe and F. Besenbacher, *Phys. Rev. Lett.*, 2000, **84**, 951–954.
- 50 H. Liu, L. Jiao, F. Yang, Y. Cai, X. Wu, W. Ho, C. Gao, J. Jia, N. Wang, H. Fan, W. Yao and M. Xie, *Phys. Rev. Lett.*, 2014, **113**, 066105.
- 51 O. Lehtinen, H. P. Komsa, A. Pulkin, M. B. Whitwick, M. W. Chen, T. Lehnert, M. J. Mohn, O. V. Yazyev, A. Kis, U. Kaiser and A. V. Krasheninnikov, *ACS Nano*, 2015, **9**, 3274–3283.